Yttrium co-precipitation with smectite: A polarized XAS and AsFlFFF study

N. Finck *, M. Bouby, K. Dardenne, T. Yokosawa

Institute for Nuclear Waste Disposal (INE), Karlsruhe Institute of Technology (KIT), P.O. Box 3640, 76021 Karlsruhe, Germany

ARTICLE INFO

Keywords:
Clay minerals
Yttrium
Polarized XAS
Nanoparticles
AsFlFFF

ABSTRACT

The Y(III) binding mechanism(s) by coprecipitation with or by adsorption on hectorite, a mineral phase frequently detected in nuclear waste glass alteration experiments, was investigated by polarized EXAFS (P EXAFS) spectroscopy. The novelty in this study is the use of yttrium to take advantage of the higher angular dependence of the absorption coefficient at the *K* edge for P EXAFS measurements. In the coprecipitation experiment, a brucite precursor was prepared in the presence of Y and subsequently aged to produce hectorite. In the adsorption experiment, Y(III) ions contacted pre formed hectorite in dispersion. The coprecipitated hectorite and brucite and the hectorite from adsorption experiment were each prepared as textured samples and the Y(III) local environment was probed by P EXAFS spectroscopy. P EXAFS analysis indicated that Y(III) is 6 fold coordinated by O atoms in both the coprecipitated brucite and the coprecipitated hectorite, and surrounded by next nearest Mg/Si shells. The angular dependences of the coordination numbers strongly point to Y(III) substituting for Mg(II) in brucite layers. Upon hectorite crystallization the local environment evolved. Mg and Si shells were detected at distances suggesting an octahedral clay like environment in the coprecipitated hectorite, and this finding was corroborated by the angular dependence of the coordination numbers. In the adsorption sample, Y(III) forms inner sphere surface complexes at the platelet edges (i.e., (0 1 0) plane), slightly tilted off the median clay plane. The presence of such surface complexes in the coprecipitation sample could not be evidenced. Finally, the supernatant of the dispersion containing the coprecipitated hectorite was analyzed by the asymmetrical flow field flow fractionation (AsFlFFF) technique coupled to ICP MS to obtain information on the smallest sized particles. The AsFlFFF data indicate that nanoparticulate hectorite of various sizes (50 75 nm, 125 140 nm and >450 nm) can be separated from the bulk dispersion and this finding was corroborated by TEM experiments on the same supernatant. Furthermore, AsFlFFF data also indicate that Y(III) behaves like Mg, used as fingerprint of the presence of hectorite. This finding suggests random substitution for octahedral cation within hectorite nanoparticles. Trivalent yttrium was used as proxy for trivalent actinides (An(III)). Consequently, this study supports the incorporation of An(III) into hectorite forming in the nuclear waste glass alteration layer in deep disposal sites, as already suggested in previous studies.

1. Introduction

Several countries (e.g., Belgium, France, Switzerland) operating nuclear power plants have decided to vitrify the high level nuclear waste (HLW) and to place the resulting glass in canisters before disposing it of in deep facilities. However, over geological timescales groundwater will move through the barriers (e.g., the clay host rock and the bentonite backfill) and come in contact with the canister containing vitrified HLW. After corrosion of the metallic canister, groundwater will ultimately come in contact with the vitrified waste which will start altering. Experiments performed over timescales of months to years at elevated temperatures have shown that glass altered in the presence of groundwater produces various neoformed secondary phases (e.g., Abdelouas et al., 1997; Zimmer et al., 2002; Thien et al., 2010), such as hectorite ($Na_{0.33}(Mg_{2.67}Li_{0.33})Si_4O_{10}(OH)_2$) (Zwicky et al., 1989; Curti et al., 2006; Thien et al., 2010; Jollivet et al., 2012). Radiotoxic and long lived radionuclides (RNs), such as the actinides (Ans), are also expected to be released upon glass alteration, however, the interaction with alteration phases is expected to hinder the migration of these RNs out of the repository site. Several interaction mechanisms can contribute to retention, such as surface adsorption and incorporation within the crystal lattice of minerals. Adsorption of cations at the solid/liquid interface has been extensively studied in the past and a thorough review is given in Geckeis et al. (2013). Based on these studies, surface complexation models could be developed (e.g., Bradbury and Baeyens, 2002). The formation of alteration phases in the presence of Ans makes entrapment of these species within the bulk structure possible,

* Corresponding author.
E-mail address: nicolas.finck@kit.edu (N. Finck).

resulting in most efficient immobilization, especially if a solid solution forms (Kim and Grambow, 1999). However, despite the abundance of solid solutions in natural systems, reliable models to predict their for mation are hardly available. The development of such models relies on molecular scale information provided by specific laboratory experi ments using advanced spectroscopic techniques.

Structural incorporation of trivalent Ans, or of their non radioactive chemical surrogates the lanthanides (Lns), within various mineral phases has been reported (e.g., Pieper, 2005; Dardenne et al., 2002; Bosbach et al., 2004; Schlegel et al., 2004; Stumpf et al., 2006, 2007; Finck et al., 2009, 2012, 2015a) but only few studies were dedicated to the incorporation of Ln(III)/An(III) within smectites. For example, the preparation of hectorite in the presence of Lu(III) following a multi step synthesis protocol resulted in an incorporation of the lanthanide within the smectite octahedral sheet (Finck et al., 2009). Following a similar protocol, hectorite was prepared in the presence of Eu(III) (Pieper, 2005; Finck et al., 2012) or Am(III) (Finck et al., 2015a). In these studies, the site distortion originating from the size mismatch be tween Eu(III) ($r(^{VI}Eu(III)) = 0.95$ Å) or Am(III) ($r(^{VI}Am(III)) = 0.98$ Å) and cations typically occurring at octahedral site (e.g., $r(^{VI}Al(III)) =$ 0.54 Å, $r(^{VI}Mg(II)) = 0.72$ Å, $r(^{VI}Fe(III)) = 0.65$ Å, $r(^{VI}Fe(II)) =$ 0.78 Å) made difficult the structural characterization of the incorporat ed species. Yet, powder X ray absorption spectroscopy (XAS) data indi cated that some Eu(III) or Am(III) is located in a hectorite like octahedral environment, and that some Eu(III) or Am(III) is also present as surface adsorbed species certainly as a consequence of a limited structural compatibility. Similar findings were reported by Brandt et al. (2007) using laser fluorescence spectroscopy to probe the local envi ronment of Cm(III) during coprecipitation with hectorite. The applica tion of powder EXAFS spectroscopy in the above mentioned studies was also complicated by interferences of EXAFS waves scattered by neighboring shells located at similar distances from the absorber. This is typical in clay minerals where absorbing atoms of the octahedral sheet are surrounded by cationic backscatterers located in the octahe dral ($R \sim 3.05$ 3.10 Å) and tetrahedral ($R' \sim 3.20$ 3.25 Å) sheets. The EXAFS contributions of these shells may overlap, thus complicating the characterization of the local environment of the probed cation. This complication can be overcome by application of polarized EXAFS (P EXAFS) spectroscopy on clay minerals prepared as highly textured samples (e.g., Schlegel et al., 1999; Dähn et al., 2002; Finck et al., 2009).

The theoretical background and principle of P EXAFS spectroscopy is well documented (e.g., Manceau et al., 1990, 1998; Schlegel et al., 1999) and summarized in the Supplementary Content. Briefly, contributions of absorber backscatterer pairs with distinct crystallographic orientations can be discriminated from the orientation of the clay film with respect to the X ray beam. The contribution from cations in the octahedral sheet is maximized when the experimental angle (α) between the hectorite layer plane and the electric field of the X ray beam equals 0°, and minimized when $\alpha = 90°$. The opposite angular dependence is ob served for cations located in the tetrahedral sheet. Furthermore, at the K edge, the relationship between the apparent coordination number (N^{app}) and the (isotropic) coordination number for a perfectly disor dered powder (N^{pwdr}) is: N^{app} $N^{pwdr}[1-\frac{(3\cos^2\beta\ 1)(3\cos^2\alpha\ 2)}{2}]$, where β is the angle between the vector connecting the absorber to the backscat ter and the layer normal. Thus, P EXAFS can provide unique information on the nature, number, distance and orientation of neighboring shells.

In XAS experiments, information on the speciation of lanthanides and actinides is usually obtained by probing their L_3 edge (e.g., Eu ($E = 6977$ eV), Lu ($E = 9244$ eV), Am ($E = 18{,}510$ eV)), mostly because these energies can be accessed more easily than that of the K edge of these elements (e.g., Eu ($E = 48{,}519$ eV), Lu ($E = 63{,}314$ eV), Am ($E = 124{,}982$ eV)). Unfortunately, the angular dependence of the ab sorption coefficient at the L_3 edge is much weaker (about 3 times) than at the K edge (Manceau et al., 1998; Schlegel and Descostes, 2009, Supplementary Content). Fortunately, yttrium is of same oxidation state (+III) and of size (Shannon, 1976) ($r(^{VI}Y(III)) =$ 0.90 Å) comparable to that of lanthanides (e.g., $r(^{VI}Lu(III)) =$ 0.86 Å; $r(^{VI}Eu(III)) = 0.95$ Å). Furthermore, the K edge of yttrium ($E = 17{,}038$ eV) is located at significantly lower energy than that of the Lns and thus is more easily accessible. Earlier P EXAFS data in dicated that Lu(III) can occupy hectorite octahedral sites, but Lu(III) is slightly smaller than trivalent actinides (e.g., $r(^{VI}Am(III)) = 0.98$ Å, $r(^{VI}Cm(III)) = 0.97$ Å), whereas Y(III) has a size more comparable with these ions. Thus, using Y(III) as surrogate for Ln(III)/An(III) combines several advantages (similar chemical properties and size, and more easily accessible K edge) and the application of P EXAFS spectroscopy will enable to unambiguously decipher the actual bind ing mode in hectorite coprecipitation experiments.

Yttrium is a member of the rare earth family and the concentration of these elements within naturally occurring smectites is often used to obtain information on the possible formation mechanism (e.g., Severmann et al., 2004; Dekov et al., 2007). However, no spectroscopic characterization by directly probing Y(III) structurally bound within smectite has been reported so far. This study is the first to report spec troscopic data on Y(III) incorporated within smectite prepared in the laboratory and this sample can be considered as model system for nat urally occurring smectites.

Secondary phases formed upon glass alteration by groundwater are of various sizes. Whether forming by direct precipitation (homoge neous nucleation) or, more likely, by precipitation on a previously existing solid phase (heterogeneous nucleation) (Meunier, 2005), the crystallites are of small sizes in the early stages and can be defined as colloids or nanoparticles (NP). Because of their small sizes, NP are po tentially highly mobile (e.g., Novikov et al., 2006; Utsunomiya et al., 2009; Crançon et al., 2010) and thus may serve as vehicles for the migra tion of low soluble RNs whether located within the bulk structure or adsorbed at the surface. The application of asymmetrical flow field flow fractionation (AsFlFFF) has proven to be a powerful tool in the characterization of NP. AsFlFFF is a chromatography like technique used to separate NP as a function of their sizes, and when coupled to sensitive detection techniques (e.g., ICP MS) can provide information on the elemental composition as a function of the size. The theoretical background of AsFlFFF and the coupling to sensitive detection tech niques is well documented (e.g., Hassellöv et al., 1999; Schimpf et al., 2000; Bouby et al., 2008; Dubascoux et al., 2008). Recently, AsFlFFF coupled to ICP MS has been applied to study the interaction of Lu(III), Eu(III) or a mixture of lanthanides (La(III), Eu(III) and Yb(III)) (Bouby et al., 2015) with hectorite. Analysis of NP mobilized from the bulk hectorite synthesized in the presence of Lu(III) (Bouby et al., 2012) in dicated a homogeneous Lu(III) association (incorporation) to hectorite over the whole size range (17 200 nm). In another study, hectorite was synthesized in the presence of Eu(III) and NP were separated from the bulk dispersion. The application of AsFlFFF/ICP MS and EXAFS spectroscopy to analyze the same sample indicated that Eu(III) can be structurally retained within NP but less homogeneously (mix ture of incorporated and surface adsorbed species) than the slightly smaller Lu(III) (Finck et al., 2012).

In the present study, the Y(III) retention mechanism(s) upon coprecipitation with or adsorption onto hectorite were investigat ed. In the coprecipitation experiment, hectorite was crystallized from a brucite precursor that was synthesized in the presence of Y(III). In the adsorption experiment, Y(III) ions contacted pre formed hectorite in dispersion. P EXAFS spectroscopy was used to characterize the Y(III) binding mode at different stages of the hectorite crystallization, and the adsorption sample was used as ref erence to distinguish structural incorporation from surface adsorp tion. For hectorite prepared in the presence of Y(III), NP were also separated from the bulk dispersion and analyzed by AsFlFFF/ICP MS in order to provide insight(s) into the Y(III) binding mode for the smallest sized particles. The size of these particles was also checked by TEM.

Table 1
Description of the samples used in this study.

Sample name	Sample preparation	Sample type	Y(III) content
YcopBru	Brucite synthesized in the presence of Y(III)	Self-supporting film	1.6 mg/g
YcopHt	Hectorite crystallized from a brucite precursor synthesized in the presence of Y(III)	Self-supporting film	3.3 mg/g
ColYcopHt	Centrifugation of YcopHt dispersion, dilution in eluent	Dispersion	0.02 mg/L
YadsHt	Y(III) adsorbed onto hectorite: 2 g/L hectorite in 0.5 mol/L NaCl, [Y(III)] = 50 μmol/L, pH = 7.7(1)	Self-supporting film	2.2 mg/g

2. Materials and methods

2.1. Samples preparation

All samples (Table 1) and reference compounds were prepared with ultra pure water (18.2 MΩ·cm, Milli Q system, Millipore) and reagents of ACS grade or higher. An Y(III) stock solution ([Y(III)] = 0.1 mol/L, sample $Y(III)_{aq}$) was prepared by dissolving Y_2O_3 (Alfa Aesar REacton 99.995% (REO)) in $HClO_4$. Hectorite was synthesized in the presence of Y(III) (sample YcopHt) following a multi step synthesis protocol (Finck et al., 2009). An Y(III) containing brucite precursor phase was freshly precipitated and washed several times with ultra pure water. The resulting slurry was refluxed (100 °C) in the presence of LiF and a silica sol (Ludox HS 30, Aldrich) to crystallize hectorite. The resulting smectite was washed at pH ~3 (HCl) and subsequently thoroughly with ultra pure water prior to further analysis. In a separate experiment, Y(III) ions were adsorbed onto pre formed pure hectorite in dispersion (m/V = 2 g/L, 0.5 mol/L NaCl, [Y(III)] = 50 μmol/L, pH = 7.7 ± 0.1 (thereafter the condensed notation 7.7(1) is used for uncertainties), 2 days contact time ensuring quantitative uptake, sample YadsHt). Separately, an Y(III) containing brucite sample (sample YcopBru) was also prepared. Samples YcopBru, YcopHt and YadsHt were prepared as self supporting films by filtering the corresponding dispersion on cellulose nitrate filters (0.025 μm pore size, Millipore). This protocol readily provided highly textured films (Schlegel et al., 1999; Dähn et al., 2002).

All solid phases were characterized by powder X ray diffraction (XRD) on oriented samples prepared by drying a small amount of slurry on a sample holder. X ray diffractograms were recorded on a D8 Advance (Bruker) diffractometer (Cu K_α radiation) equipped with an energy dispersive detector (Sol X). Phases were identified by comparison with the PDF 2 database using the DIFFRAC.EVA V3.1 software (Bruker) and fits to the data were provided by the TOPAS 4.2 software (Bruker).

Finally, part of the YcopHt dispersion was centrifuged for 35 min at 4000 rpm (Megafuge 2.0 R, Thermo Scientific, Heraeus Instrument) in order to separate the smallest sized particles (i.e., the NP) for analysis by AsFlFFF/ICP MS. The supernatant obtained by centrifugation contained 0.2 mg/L Y and 56.7 mg/L Mg (Mg:Y mass ratio of 284). The supernatant was diluted ten times in eluent shortly before injection to avoid saturation of the detectors, this protocol formed sample ColYcopHt. Unfortunately, the Y content in the supernatant before dilution was too low for EXAFS measurements.

2.2. X ray absorption spectroscopy (XAS)

Information on the Y(III) local environment was provided by probing the *K* edge by X ray absorption spectroscopy at the INE Beamline (Rothe et al., 2012) at the synchrotron light source ANKA (Karlsruhe, Germany). The storage ring energy was 2.5 GeV and the ring current was 180 90 mA. The incident X ray beam was monochromatized using a pair of Ge(422) crystals. The energy calibration was performed by assigning the first inflection point of the Y *K* edge of an Y foil at 17,038.0 eV and this reference was measured in parallel with all samples. For samples YcopBru, YcopHt and YadsHt, the self supporting film was mounted on a goniometer and polarized XAS data were collected in fluorescence mode using a five elements LEGe solid state detector (Canberra Eurisys). Data were collected at angles α between the electric field of the X ray beam and the layer plane of $\alpha = 10°, 35°$ and 80°, and additionally at $\alpha = 55°$ for YcopBru. Powder XAS data were collected in transmission mode for the $Y(III)_{aq}$, Y_2O_3 and $Y(OH)_3$ reference compounds.

XAS data were analyzed following standard procedures by using Athena and Artemis interfaces to the Ifeffit software (Ravel and Newville, 2005). EXAFS spectra ($\chi(k)$) were extracted from the raw data and Fourier transforms (FTs) were obtained from the $k^3 \times \chi(k)$ functions. Data were fit in *R* space by using a combination of single scattering paths where phase and amplitude functions were calculated with feff8.4 (Ankudinov et al., 1998). For a given film, data were fit simultaneously at all angles, using a common value of ΔE, and for a given shell a common bond length and mean square displacement ("Debye Waller" term) (Finck et al., 2009; Schlegel and Manceau, 2013). Uncertainties on EXAFS distances and coordination numbers are indicated in parentheses in Tables 2 5, and the experimental uncertainty on α is estimated to ±1°. The fit quality was quantified by the R_f factor, representing the absolute misfit between theory and data (Ravel, 2000).

2.3. Asymmetrical flow field flow fractionation (AsFlFFF)

A detailed description of the equipment used in this study (HRFFF 10.000 A4F, Postnova Analytics, Landsberg, Germany) can be found in (Bouby et al., 2008, 2011) and a summary is presented in the Supplementary Content, only a brief description is given here. The dispersion containing the nanoparticles is injected into a ribbon like channel and the components are eluted by a carrier solution (ultra pure water adjusted at pH 9.3 by addition of NaOH) while applying simultaneously a secondary perpendicular flow field (cross flow). The size calibration was done by using carboxylated polystyrene reference particles (Magsphere, USA) (Bouby et al., 2008). After fractionation, the effluent is injected into the nebulizer of an ICP MS (Perkin Elmer Elan 6000) in order to obtain information on the elemental composition as a function of the size. For calibration of the AsFlFFF/ICP MS arrangement a solution containing the elements of interest in 6% nitric acid was prepared from standard solutions.

Sample ColYcopHt was analyzed by AsFlFFF before and after filtration with a filter of 450 nm pore size diameter. The hectorite octahedral sheet mostly contains Mg which can be used as an indicator of the presence of the smectite. Information on the Y(III) binding mode with the

Table 2
Structural parameters from EXAFS analysis of reference compounds.

Sample	Path	*N*	*R* [Å]	σ^2 [Å^2]	ΔE_0 [eV]	R_f ($\times 10^3$)
$Y(III)_{aq}$	Y O	8.0	2.35(2)	0.006	4.1(12)	3.3
$Y(OH)_3$	Y O	9.0	2.40(2)	0.008	1.6(6)	5.0
	Y Y	2.0	3.54(3)	0.005		
	Y O	3.0	3.78(4)	0.005		
	Y Y	6.0	4.02(4)	0.007		
	Y O	6.0	4.38(5)	0.008		
Y_2O_3	Y O	6.0	2.27(2)	0.007	1.2(6)	6.8
	Y Y	6.0	3.52(2)	0.007		
	Y Y	6.0	3.99(4)	0.008		
	Y O	6.0	4.27(4)	0.008		
	Y O	6.0	4.46(3)	0.007		

The number in parentheses indicates the uncertainty (the coordination numbers were held fix). *R*: interatomic distance, *N*: number of neighboring atoms, σ^2: mean square displacement, ΔE_0: energy shift, R_f: figure of merit of the fit.

Table 3
Quantitative EXAFS analysis of the sample YcopBru (1.1C atom at 2.82 Å).

α	FT range[a]	Fit range[b]	Y ↔O1			Y ↔ Mg1		
	[Å ^{1}]	[Å]	*N*	*R* [Å]	σ² [Å²]	*N*	*R* [Å]	σ² [Å²]
10°	4.2–10.3	1.4–3.9	7.1(4)	2.24(2)	0.010	6.4(5)	3.25(2)	0.009
35°			6.6(4)			5.1(4)		
55°			6.2(4)			3.7(4)		
80°			5.7(4)			2.6(3)		

α	Y ↔ O2			Y ↔ O3			ΔE_0	R_f
	N	*R* [Å]	σ² [Å²]	*N*	*R* [Å]	σ² [Å²]	[eV]	(×10³)
10°	4.3(5)	3.73(5)	0.006	1.8(11)	4.14(5)	0.006	8.3(3)	14.2
35°	4.0(6)			1.8(5)				3.4
55°	3.6(5)			1.6(8)				3.8
80°	3.2(5)			1.6(5)				9.7

The number in parentheses indicates the uncertainty. [a]Fourier transformed $\chi(k)$ range. [b]$R + \Delta R$ interval for the fit. *R*: interatomic distance, *N*: number of neighboring atoms, σ²: mean square displacement, ΔE_0: energy shift, R_f: figure of merit of the fit.

smectite can be derived from the variation of the Mg:Y ratio as a function of the size (Bouby et al., 2011, 2012, 2015; Finck et al., 2012). For Y structurally incorporated within the hectorite structure, the Mg:Y ratio is expected to be constant for all particle sizes. For Y(III) adsorbed at the surface of hectorite, the NP associated amount of Y(III) is expected to follow the surface area to volume ratio, and thus the Mg:Y ratio is expected to change with the NP size (Bouby et al., 2015).

3. Results and interpretations

3.1. X ray diffraction

The X ray diffractogram of $Y(OH)_3$ could be modeled (Fig. 1) considering only the structure reported by Beall et al. (1977), no separate phase was detected. The X ray diffractogram of YcopBru indicated the presence of only magnesium hydroxide, and a good fit to the data was obtained considering only brucite. The presence of trace amounts of Y(III) had only marginal influence on the lattice parameters of YcopBru ($a = 3.15891(25)$ Å, $c = 4.78064(39)$ Å) compared to brucite synthesized in the absence of Y(III) ($a = 3.14724(17)$ Å, $c = 4.77614(48)$ Å, data not shown) and to reported crystallographic data ($a = 3.1498(0)$ Å, $c = 4.7702(1)$ Å (Catti et al., 1995)). The X ray diffractogram of YcopHt is similar to that reported for pure hectorite (Finck et al., 2012). No other crystalline phase could be detected, indicating that only marginal amount of brucite precursor phase may be present and that no by product formed. Note that the diffraction peak centered at ~61°2θ and corresponding to $d(060)$ ~ 1.52 Å is consistent with a trioctahedral smectite.

3.2. X ray absorption spectroscopy (XAS)

3.2.1. X ray absorption near edge structure (XANES)

The edge crest or white line (WL) of the Y_2O_3 spectrum has a double peak structure (Fig. 2) with maxima at 17,053.0(3) and 17,060.0(3) eV, and earlier work suggested such line shape originates from Y located at two different sites (Malvestuto et al., 2005). In contrast, the XANES of all other compounds (reference compounds and samples at $\alpha = 35°$) contain only one single edge crest, indicating the presence of only one equivalent site. Furthermore, the maximum of the first oscillation after the WL in the reference compounds is located at different energies: 17,100.0(4) eV for $Y(OH)_3$, 17,105.0(4) eV for $Y(III)_{aq}$ and 17,110.0(4) eV for Y_2O_3. This increase in energy position can be attributed to a decrease in interatomic distance from Y to the first O shell (Bianconi et al., 1983) and will be verified by fits to the EXAFS data. The XANES of YcopBru, YcopHt and YadsHt differ from those of the reference compounds, indicating that these references are not a major component of the samples. For example, the WL of the samples is of lower intensity than in $Y(OH)_3$ and $Y(III)_{aq}$. For YcopBru, the maximum of the first oscillation after the WL is located at 17,112.0(4) eV and indicates a short Y O interatomic distance. This oscillation also contains an additional feature at 17,092.7(4) eV which is absent in the other samples, hinting at a specific environment in YcopBru. Besides, it also indicates that no detectable amounts of YcopBru precursor is present in YcopHt, which is in agreement with XRD data. The XANES of YcopHt and YadsHt look similar suggesting that Y(III) is surrounded by similar type of backscatterers (i.e., Mg and Si atoms) at similar distances in both samples.

The polarized XANES (Fig. 3) of YcopBru exhibit a significant angular dependence over the whole energy range, and well defined isosbestic points are observed, attesting for the high degree of particles orientation within the film and for the reliability of the data reduction. The variation in amplitude and position of the WL and the first oscillation centered at ~ 17,112 eV are consistent with a highly anisotropic environment. The probed Y *K* edge corresponds to a $1s \rightarrow 5p$ transition, which is dichroic in nature, and together with the polarization dependence attest for the successful preparation of highly oriented films. The presence of Y precipitates or polymers can be ruled out because they would not lead to angular dependent spectra. The XANES of YcopHt and YadsHt also exhibit angular dependences, though of lower amplitude because of possible partial misorientation of individual hectorite platelets, indicating that Y(III) is structurally connected to a mineral phase and located in an anisotropic environment in these samples. Note that XAS data were treated in a consistent way (see also Supporting Content) and thus small differences in the spectra are significant and do not originate from data treatment.

3.2.2. Extended X ray absorption fine structure (EXAFS) of reference compounds

The EXAFS spectrum of $Y(III)_{aq}$ contains a single wave frequency of decreasing amplitude for $k > 4$ Å^{-1}, consistent with the presence of

Table 4
Quantitative EXAFS analysis of the sample YcopHt.

α	FT range[a]	Fit range[b]	Y ↔ O1			Y ↔ O2			Y ↔ Mg1		
	[Å ^{1}]	[Å]	*N*	*R* [Å]	σ² [Å²]	*N*	*R* [Å]	σ² [Å²]	*N*	*R* [Å]	σ² [Å²]
10°	4.1–8.2	1.3–4.3	2.0(3)	2.20(2)	0.005	3.6(3)	2.37(2)	0.005	2.4(5)	3.34(3)	0.006
35°			2.1(3)			3.3(3)			1.8(4)		
80°			2.3(2)			2.9(2)			1.4(5)		

α	Y ↔ Si1			Y ↔ Si2			ΔE_0	R_f
	N	*R* [Å]	σ² [Å²]	*N*	*R* [Å]	σ² [Å²]	[eV]	(×10³)
10°	2.9(5)	3.50(4)	0.006	1.0(6)	4.41(5)	0.005	1.5(4)	5.1
35°	2.8(4)			1.0(8)				9.4
80°	3.7(3)			1.2(7)				3.2

The number in parentheses indicates the uncertainty. [a]Fourier transformed $\chi(k)$ range. [b]$R + \Delta R$ interval for the fit. *R*: interatomic distance, *N*: number of neighboring atoms, σ²: mean square displacement, ΔE_0: energy shift, R_f: figure of merit of the fit.

Table 5
Quantitative EXAFS analysis of the sample YadsHt.

α	FT range[a]	Fit range[b]	Y ↔ O1			Y ↔ O2			Y ↔ Mg1		
	[Å ^{1}]	[Å]	*N*	*R* [Å]	σ² [Å²]	*N*	*R* [Å]	σ² [Å²]	*N*	*R* [Å]	σ² [Å²]
10°	4.0–9.2	1.3–3.9	3.0(2)	2.25(2)	0.003	3.2(2)	2.43(2)	0.003	0.4(3)	3.08(4)	0.006
35°			3.1(2)			3.2(2)			0.5(3)		
80°			3.0(3)			2.6(2)			0.7(4)		

α	Y ↔ Si1			Y ↔ Si2			ΔE_0	R_f
	N	*R* [Å]	σ² [Å²]	*N*	*R* [Å]	σ² [Å²]	[eV]	(×10³)
10°	0.8(3)	3.51(4)	0.006	0.9(6)	4.01(6)	0.006	0.1(4)	12.3
35°	0.9(3)			1.0(5)				10.0
80°	1.3(4)			0.6(4)				6.8

The number in parentheses indicates the uncertainty. [a]Fourier transformed $\chi(k)$ range. [b]$R + \Delta R$ interval for the fit. *R*: interatomic distance, *N*: number of neighboring atoms, σ²: mean square displacement, ΔE_0: energy shift, R_f: figure of merit of the fit.

only one ordered shell (Fig. 2). Accordingly, the FT contains only one peak at $R + \Delta R$ ~ 1.85 Å, corresponding to O atoms from the first hydration shell. A good fit was obtained with one shell of $N_{O1} = 8.0$ O atoms at $d(Y\ \ O1) = 2.35(2)$ Å (Fig. 2, Table 2), in good agreement with reported data (Díaz Moreno et al., 2000). The spectra of Y_2O_3 and $Y(OH)_3$ contain spectral features that are absent in $Y(III)_{aq}$ and indicate the presence of multiple ordered shells. The corresponding FTs contain various contributions at $R + \Delta R$ ~ 1.80, 3.10 and 3.65 Å which could be modeled considering Y and O backscatterers with coordination numbers and interatomic distances matching reported crystallographic data (Fig. 2, Table 2) (Beall et al., 1977; Mitric et al., 1997).

3.2.3. EXAFS of yttrium coprecipitated brucite

The powder EXAFS spectrum (i.e., at $\alpha = 35°$) of YcopBru differs from that of the reference compounds in both amplitude and position of the oscillation maxima at e.g., k ~ 7 Å^{-1} and k > 8.5 Å^{-1} (Fig. 2). The P EXAFS spectra of YcopBru (Fig. 3) exhibit a significant angular dependence over the whole k range and well defined isosbestic points are observed. The high angular dependence is indicative of Y(III) located in an anisotropic environment and thus of the presence of multiple atomic shells having distinct orientations. The FT contains a first peak at $R + \Delta R$ ~ 1.70 Å corresponding to the first O shell, and additional peaks are present at ~2.5 and ~3.2 Å corresponding to higher distances Mg and O shells. The FTs exhibit high angular dependence and the decrease in amplitude maxima with increasing α values hints at an in plane orientation of neighboring shells. The FT peak at $R + \Delta R$ ~ 6.0 Å is located at twice the distance of that centered at ~3.0 Å corresponding to neighboring Mg atoms, and can be attributed to the next octahedral shell (further supported by the angular dependence). This peak is amplified in trioctahedral structures (i.e. in an octahedral sheet where all sites are filled with divalent cations, as in brucite) by a shadowing (focusing) multiple scattering effect (Teo, 1986). This multiple scattering path is absent in dioctahedral structures (i.e. in an octahedral sheet where only two thirds of sites are filled with trivalent cations, as in gibbsite) because of the existence of vacancies that break the focusing of the electronic waves (Manceau et al., 1998). This finding strongly points to Y(III) located within brucite octahedral sheet with neighboring octahedral sites filled with Mg atoms.

A good fit to the first FT peak was obtained with one O shell at $d(Y\ \ O1) = 2.24(2)$ Å (Table 3) containing $N_{O1} = 6.6(4)$ atoms. Compared to the reference compounds, these distance and coordination number are within uncertainties in agreement with an octahedral environment. For α increasing from 10° to 80° N_{O1} decreases from 7.1(4) to 5.7(4) (Fig. 4, Table 3). This variation indicates that the angle between the vector connecting Y and O1 backscatterers and the layer normal (β_{O1}) is >54.7° and thus that the coordination polyhedron is flattened. This flattening can be quantified by β_{O1} from the relation $N^{app}/N^{pwdr} = 1.5(1 - 3cos^2\beta)cos^2\alpha + (3cos^2\beta)$. N^{pwdr}, the coordination number

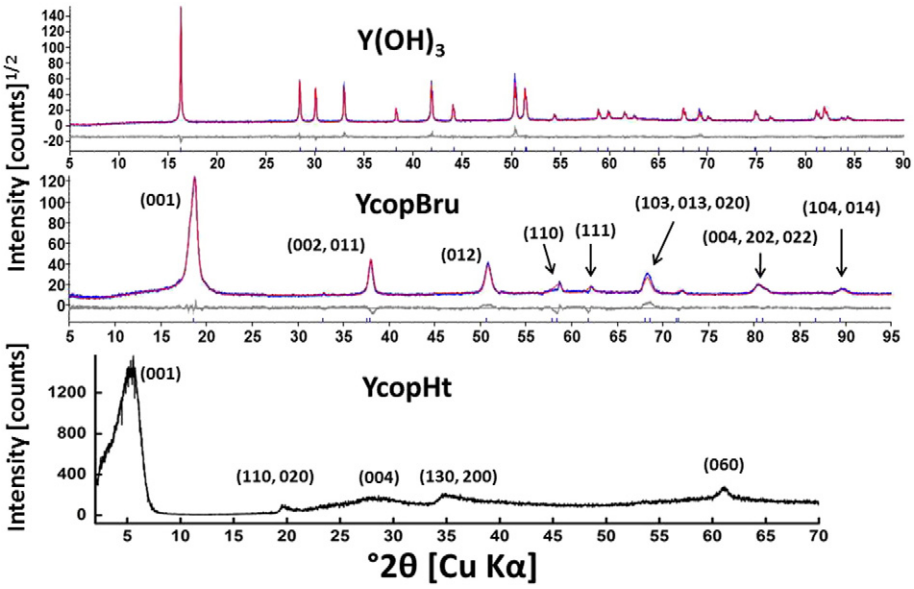

Fig. 1. X-ray diffractogram of samples $Y(OH)_3$ (up), YcopBru (middle) and YcopHt (bottom). The blue line in $Y(OH)_3$ and YcopBru represents the experimental data, the red line is the modeled data and the grey line is the difference between experimental and modeled data. The number in parentheses indicate the lattice plane.

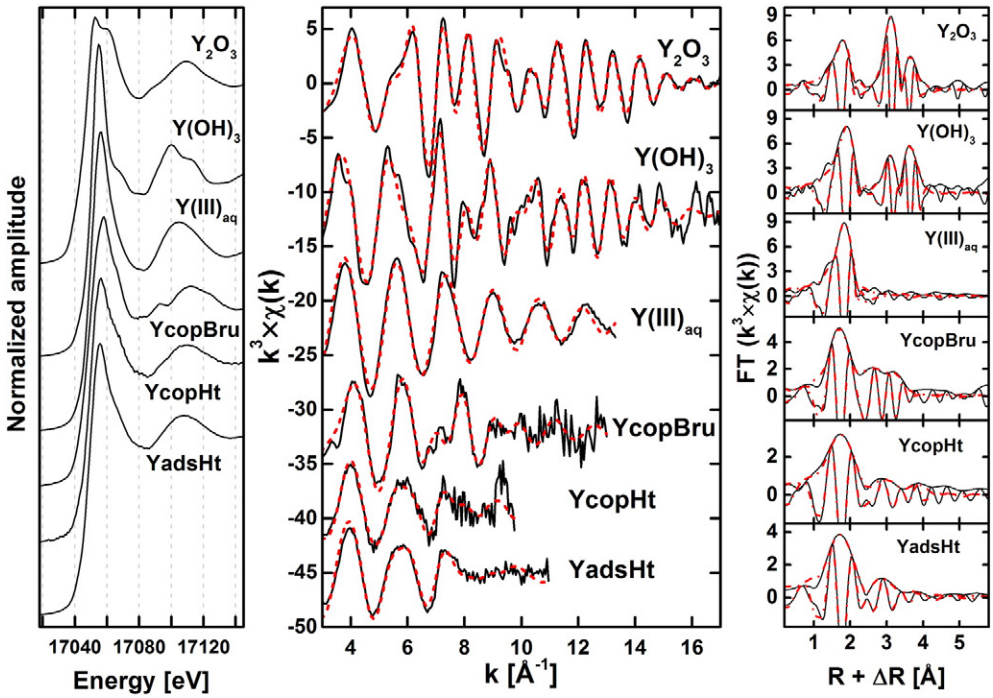

Fig. 2. Powder XAS data of all samples (i.e., data recorded at $\alpha = 35°$) and reference compounds. Left: experimental XANES spectra. Middle: experimental (solid black line) and modeled (dashed red line) EXAFS spectra. Right: experimental (solid black line) and modeled (dashed red line) Fourier transforms (amplitude and imaginary parts). Fit results are presented in Tables 2, 3, 4 and 5.

at $\alpha = 35.3°$, was first calculated from the regression of N_{O1} as a function of $cos^2\alpha$, and then $\beta_{O1}$was determined from the slope of the linear re gression of N^{app}/N^{pwdr} with respect to $cos^2\alpha$ (Supplementary Content). With $N_{O1}^{pwdr} = 6.64$, calculations yield $\beta_{O1} = 58°$, and the uncertainty was estimated to $\pm 2°$. This value agrees with the reported value of $\beta_O = 59.5°$ for pure brucite (Güven, 1988).

Spectral simulations of next FT peaks indicate the presence of one Mg shell at d(Y Mg1) = 3.25(2) Å and one O shell at d(Y O2) = 3.73(5) Å, both corresponding to atoms from adjacent octahedra. d(Y Mg1) = 3.25(2) Å is larger than d(Mg Mg) = 3.15 Å in bru cite (Catti et al., 1995) but the increase in interatomic distance (0.10 Å) is smaller than the difference in ionic radius between Mg and Y (0.18 Å), meaning that the structure could accommodate the large cation. For the O2 shell, d(Y O2) = 3.73(5) Å in YcopBru matches within uncertainties d(Mg O) = 3.79 Å in brucite. Fits were also improved by addition of one O shell at d(Y O3) = 4.14(5) Å, matching the reported distance of d(Mg O) = 4.14 Å in brucite (Catti et al., 1995). For α increasing from 10° to 80°, N_{Mg1}

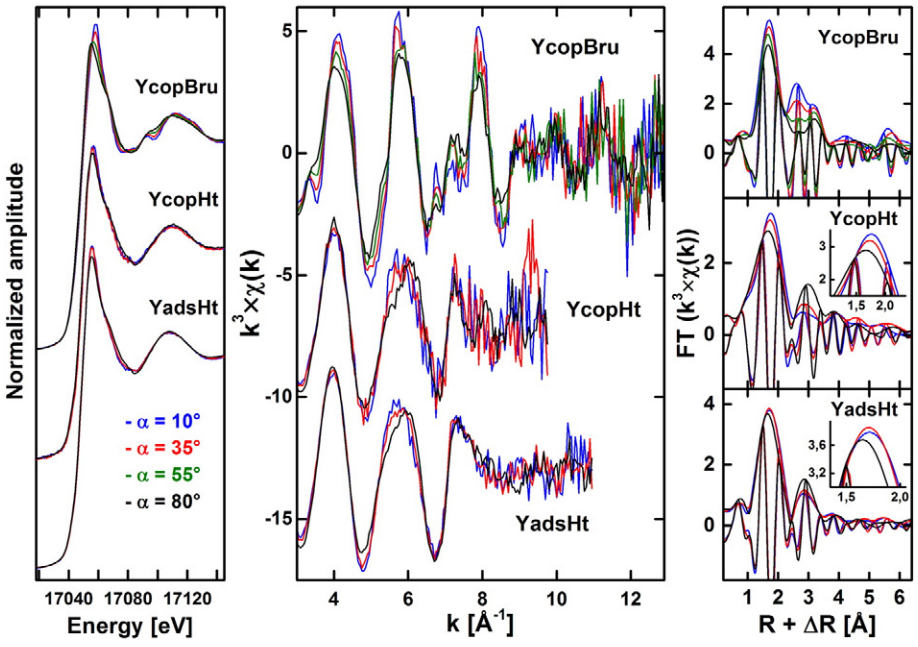

Fig. 3. Experimental polarized XAS data of samples YcopBru, YcopHt and YadsHt. Left: XANES spectra. Middle: EXAFS spectra. Right: Fourier transforms (amplitude and imaginary parts), inserts show the maxima of the FT peaks at $R + \Delta R \sim 1.7$ Å.

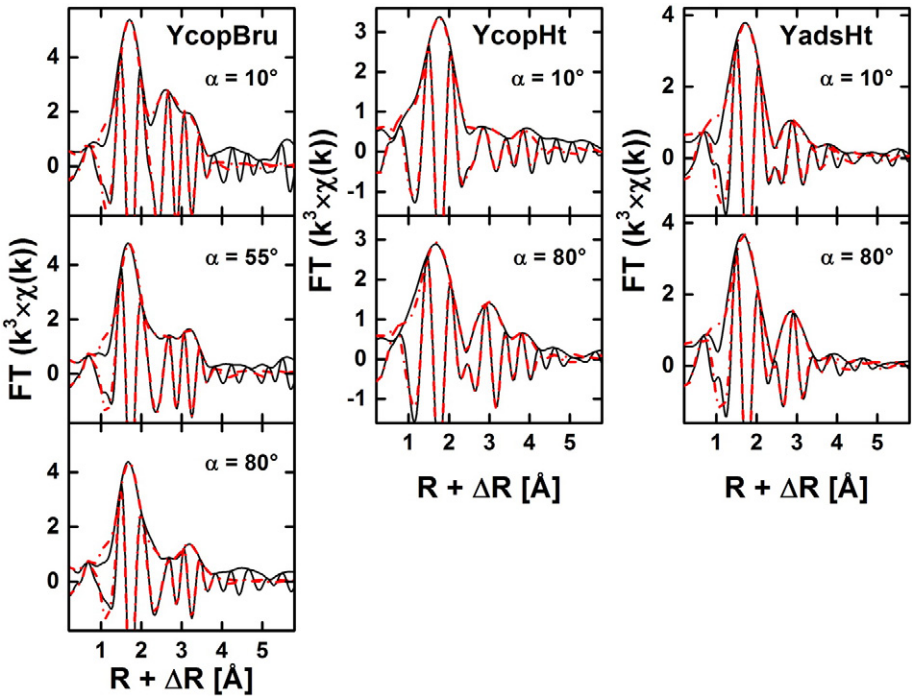

Fig. 4. Experimental (solid black line) and modeled (dashed red line) Fourier transforms for samples YcopBru (left), YcopHt (middle) and YadsHt (right) at $\alpha = 10°$ and 80°, and also $\alpha = 55°$ for YcopBru. Fit results are indicated in Tables 3, 4 and 5.

decreases from 6.4(5) to 2.6(3) and N_{O2} decreases from 4.3(5) to 3.2(5), consistent with Mg1 and O2 shells predominantly oriented in plane. For the Mg1 shell, β_{Mg1} was calculated in the same way as β_{O1}, and with $N_{Mg1}^{pwdr} = 5.11$ calculations yield $\beta_{Mg1} = 67 \pm 3°$. This value indicates that Y(III) is not located exactly at Mg octahedral site, but slightly above/below the layer plane (Fig. 5). Note that $N_{Mg1}^{pwdr} = 5.11$ is very close to the expected coordination number of six for cations at octahedral position.

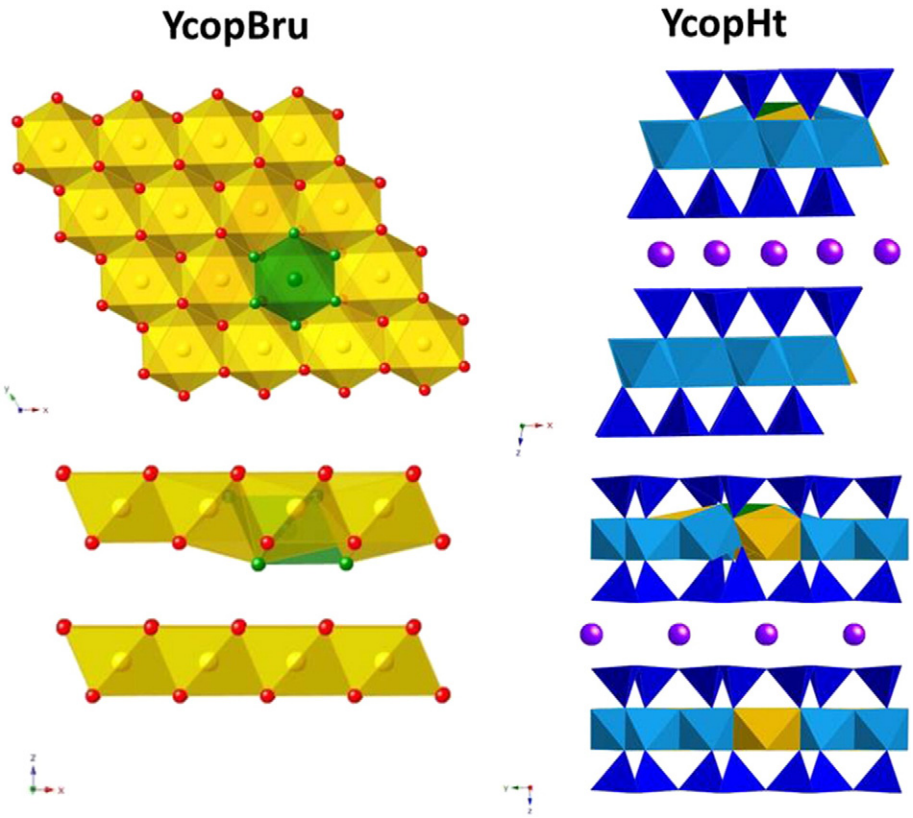

Fig. 5. Polyhedral representations of incorporated Y(III) within brucite (left) and hectorite (right).

3.2.4. EXAFS of yttrium coprecipitated hectorite

The powder EXAFS spectrum of YcopHt differs from that of YcopBru, especially at $k > 7$ Å^{-1} (Fig. 2), indicating that the local environment of Y evolved upon hectorite crystallization. The P EXAFS spectra exhibit an gular dependences, different from that of YcopBru (Fig. 3): the oscilla tions are of lower amplitude, and the maxima (e.g., at $k \sim 4$ and 5 Å^{-1}) and sometimes position (at $k \sim 6$ Å^{-1}) variations with α hint at the presence of atomic shells having distinct orientations. The FTs of YcopHt contain several peaks exhibiting angular dependences. The am plitude of the first FT peak decreases and is slightly shifted to shorter distances with increasing α values (Fig. 3), hinting at a split in two O subshells. The FTs contain an additional contribution centered at $R + \Delta R \sim 2.9$ Å, for which the peak amplitude increases with α values while the maximum is shifted from $R + \Delta R = 2.8$ to 3.0 Å, indicating the presence of more than one atomic shell.

A good fit to the first FT peak was obtained with two O shells at d(Y O1) = 2.20(2) Å and d(Y O2) = 2.37(2) Å containing in total $N_{O1} + N_{O2} = 5.4(6)$ atoms (Fig. 4, Table 4). These bond distances are shorter and larger, respectively, than d(Y O1) in YcopBru, from which YcopHt was crystallized, and the split into two subshells can be explained by the increase in size from Mg to Y. The total number of O backscatterers is within uncertainties equal to that in the precursor phase, indicating that the octahedral environment was kept upon hectorite crystallization. For α increasing from 10° to 80°, N_{O1} is within uncertainty unaffected, whereas N_{O2} slightly decreases from 3.6(3) to 2.9(2). β_{O1} and β_{O2} were calculated using the same methodology as above, and with $N_{O1}^{pwdr} = 2.10$ and $N_{O2}^{pwdr} = 3.35$ calculations (Supple mentary Content) yield $\beta_{O1} = 53 \pm 1°$ and $\beta_{O2} = 58 \pm 1°$. The value of β_{O2} is within uncertainty equal to that reported for octahedral Fe(III) within naturally occurring hectorite (Finck et al., 2015b) and also consistent with the octahedral flattening observed in most hydrous phyllosilicates (Güven, 1988).

At higher distances, a good fit was obtained with one Mg shell at d(Y Mg1) = 3.34(3) Å and one Si shell d(Y Si1) = 3.50(4) Å. These shells are located at larger distance than in hectorite (d(Mg Mg) = 3.04 Å, d(Mg Si) = 3.25 Å, (Seidl and Breu, 2005)), and the increase in bond lengths (0.25 0.30 Å) can be explained by the difference in ionic radius between Mg and Y. Furthermore, d(Y Mg1) = 3.34(3) Å in YcopHt equals the mean value of distances calculated for Y and Mg polyhedra sharing edges of d(O O)$_E$ = 2.84 Å considering either the O1 shell (d(Y Mg) = 3.20 Å) or the O2 shell (d(Y Mg) = 3.42 Å). Also, d(Y Mg1) in YcopHt is very similar to that in YcopBru, supporting that the octahedral environment was kept during hectorite crystalliza tion. The detection of the Si1 shell at d(Y Si) = 3.50(4) Å, can best be explained by Si tetrahedra condensing onto the distorted octahedral sheet in close proximity to Y centers. Fits were also improved by addition of one possible Si shell at d(Y Si2) = 4.41(5) Å, matching the reported distance of d(Mg Si) = 4.46 Å in hectorite (Seidl and Breu, 2005).

For α increasing from 10° to 80°, N_{Mg1} decreases from 2.4(5) to 1.4(5), whereas N_{Si1} increases from 2.9(5) to 3.7(3). For these two shells, calculations (Supporting Content) yield $\beta_{Mg1} = 62 \pm 10°$ (with $N_{Mg1}^{pwdr} = 1.95$) and $\beta_{Si1} = 50 \pm 5°$ (with $N_{Si1}^{pwdr} = 3.01$), indicating pref erential in plane orientation of the Mg1 shell and out of plane orienta tion of the Si1 shell. This result indicates that Y(III) is located at hectorite octahedral site but shifted in the out of plane direction (Fig. 5). Note that β_{Mg1} in YcopHt is within uncertainties equal to that in YcopBru ($\beta_{Mg1} = 67 \pm 3°$).

For the Mg1 shell, the coordination number ($N_{Mg1}^{pwdr} = 1.95$) is lower than expected for cations at octahedral position in hectorite and also lower than in YcopBru ($N_{Mg1}^{pwdr} = 5.11$). Several explanations could pos sibly explain this low N_{Mg1}. First, YcopHt contains Li(I), which is too light to be detected by XAS and the impact of this substitution on N_{Mg1} can be estimated from the Mg:Li ratio of ~8:1 in hectorite. Assum ing random distribution of Mg and Li in the octahedral sheet, the num ber of detected Mg neighbors should be close to 5.2, still significantly higher than the experimental value. Second, Y(III) substitutes for Mg(II) and the increase in local charge may be balanced by vacancies, or more likely by Li(I) preferential insertion in adjacent octahedral sites, thereby lowering the number of detected octahedral neighbors. A third hypothesis is that some Y(III) is adsorbed at the surface of hectorite, and because the number of neighboring cations for species lo cated at the surface is lower than for species located within the struc ture, the number of detected Mg atoms is lower than the expected value for cations at octahedral positions. However, the number of de tected octahedral neighbors of Y in YcopHt is within uncertainty equal to that reported for octahedral Fe(III) within naturally occurring hectorite (Finck et al., 2015b), strongly pointing to Li(I) preferential in sertion into adjacent octahedral sites in YcopHt.

3.2.5. EXAFS of yttrium adsorbed on hectorite

The powder EXAFS spectrum of YadsHt differs from that of both other samples and also from that of the reference compounds, especially at $k > 6.5$ Å^{-1} (Fig. 2). Compared to YcopHt, the first FT peak in YadsHt is narrower and of slightly higher amplitude, and compared to the Y(III)$_{aq}$ and Y(OH)$_3$ references, the first FT peak amplitude is clearly of lower in tensity in the adsorption sample. The P EXAFS spectra exhibit small but significant angular dependences (Fig. 3). The oscillation amplitudes (e.g., at $k \sim 4$ and ~4.8 Å^{-1}) and sometimes position (e.g., at $k \sim 6$ Å^{-1}) vary with α, indicating the presence of atomic shells with distinct orien tations, and thus that Y(III) is structurally connected to a solid phase. The first FT peak corresponds to O atoms and its amplitude increases for $\alpha =$ 10° to $\alpha = 35°$ and then decreases for increasing α values and at the same time the position is shifted to lower $R + \Delta R$ values. This behavior indi cates a split into two subshells having distinct orientations and suggests different Y—O bonds, as observed when some O atoms belong to the ad sorbent surface and some to bound water molecules (Schlegel, 2008; Finck et al., 2009). The FTs contain an additional contribution centered at $R + \Delta R \sim 2.9$ Å, for which the amplitude increases with α values.

A good fit to the first FT peak was obtained with two O subshells at d(Y O1) = 2.25(2) Å and d(Y O2) = 2.43(2) Å containing ~3 O atoms each (Fig. 4, Table 5). Fit results indicate that N_{O1} is unaffected whereas N_{O2} only hardly decreases for increasing α values. For these two subshells, calculations (Supporting Content) yield $\beta_{O1} = 55 \pm 2°$ (with $N_{O1}^{pwdr} = 3.04$) and $\beta_{O2} = 58 \pm 3°$ (with $N_{O2}^{pwdr} = 3.07$), indicating that both subshells are located at or close to the "magic angle" for which the apparent coordination number has no angular dependence. The next FT contribution was modeled considering Mg and Si shells at d(Y Mg1) = 3.08(4) Å and d(Y Si1) = 3.51(4) Å containing a low number of atoms (<1 Mg atom and ~1 Si atom). For increasing α values, N_{Mg1} is almost unaffected whereas N_{Si1} increases. These results are very similar to those reported for Y(III) adsorbed at edge sites of naturally oc curring hectorite at slightly lower pH values (pH 6.5 7.0) (Schlegel, 2008). Consequently, it can be concluded that Y(III) is located at edge sites in YadsHt, where Y and Mg octahedra share edges, and that Y(III) is also slightly tilted off the median hectorite plane (a graphical repre sentation can be found in (Schlegel, 2008)). No neighboring Y was de tected in YadsHt.

3.3. Asymmetrical flow field flow fractionation (AsFlFFF)

The experimental Mg and Y ICP MS fractograms obtained for the original and the filtered sample ColYcopHt are presented in Fig. 6. Before filtration, Mg and Y fractograms indicate a multimodal size distribution of smectite particles with at least three modes (peak maxima and shoul der at ~600, 750 and 900 s). The fractograms are also highly correlated and the elemental recoveries are within uncertainties equal: (61 ± 1) % for Mg and (64 ± 3) % for Y. The Mg:Y ratio is thus constant for all sizes (mass ratio of 289 ± 33), indicating a homogeneous Y(III) association to the hectorite particles (Bouby et al., 2015). The mass ratio of 289 ± 33 is within uncertainties also equal to that of the supernatant obtained by centrifugation (284) indicating the absence of any dissolved Mg or Y species.

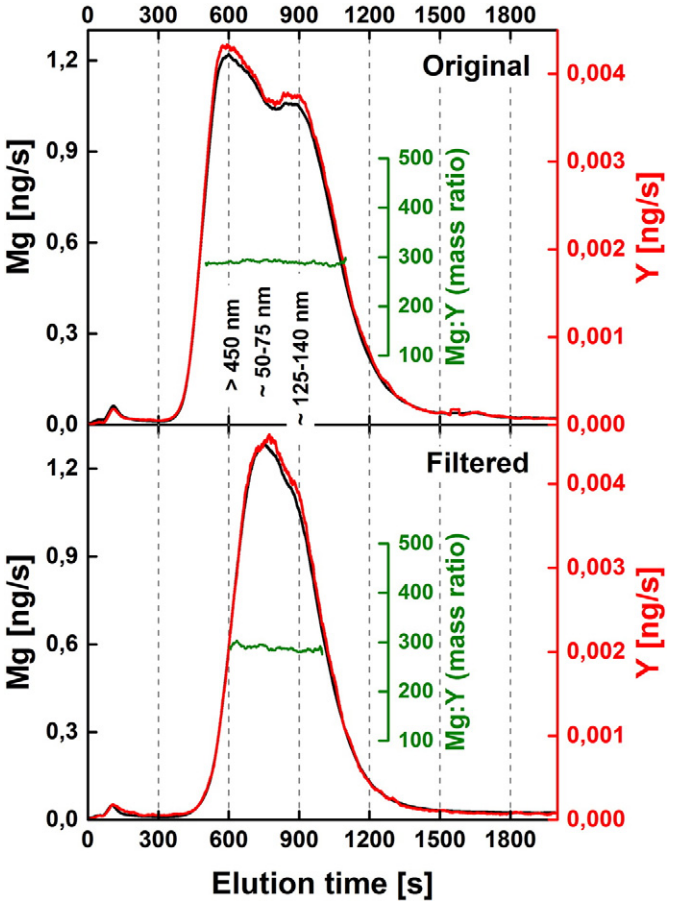

Fig. 6. Experimental Mg- (black line) and Y- (red line) ICP-MS fractograms of ColYcopHt, with the corresponding Mg:Y mass ratio (green line). Data from the original sample before filtration (up) and after filtration with filter of 450 nm pore size diameter (bottom).

After filtration, the peak at ~600 s is no longer present, the total size distribution became narrower and the fractograms are still highly correlated (Fig. 6). This indicates that the peak at ~600 s can be related to particles of sizes >450 nm. Based on the size calibration, the peaks at ~750 and 900 s correspond to size fractions of 50 75 and 125 140 nm, respectively. Furthermore, the filtration removed similar proportions of Mg ((13 ± 1) %) and Y ((15 ± 3) %), and the high correlation of the fractograms of the filtered sample indicates a homogeneous Y(III) association to hectorite particles for sizes >450 nm. The Mg:Y ratio for sizes <450 nm is also constant and within uncertainties equal to that before filtration (mass ratio of 288 ± 43). It can thus be concluded that the Mg:Y ratio is similar in all three size fractions and that Y behaves like elements of the hectorite structure. In ColYcopHt (i.e., the smallest size fraction of the hectorite dispersion), Y(III) is homogeneously associated with the hectorite and this finding can best be explained by a random Y substitution for Mg within the structure. The presence of substantial amounts of surface adsorbed Y(III) or of polymers can be excluded, because these would have led to variations in the Mg:Y ratio with the particle size. Note that size fractions of 50 75 nm and 125 140 nm compare well with values reported for hectorite synthesized in the presence of trivalent lanthanides (Bouby et al., 2012, 2015; Finck et al., 2012). The supernatant before dilution was also used for investigations by transmission electron microscopy (TEM) to support information on size and shape of the NP (Supplementary Content) and results corroborate the size distribution obtained by AsFlFFF.

4. Discussion

4.1. Fate of yttrium during brucite precursor synthesis

Trivalent yttrium was taken up during brucite synthesis and data indicate that it had no influence on the synthesis. Fits to the polarized XAS data indicate that Y(III) is located at octahedral site substituting for Mg, but slightly shifted in the out of plane direction. Furthermore, the substitution resulted in large lattice distortion, as attested by the Debye Waller term of the O1 ($\sigma^2 = 0.010$ Å^2) and Mg1 ($\sigma^2 = 0.009$ Å^2) shells. The resulting excess positive charge can be balanced by different ways. The first hypothesis is that Y(III) substitutes for Mg(II), and adjacent octahedra may be vacant for local charge balance. Alternatively, the local excess charge may be balanced by anionic species (i.e. Cl^-) located at the basal plane. However, the FT contribution at $R + \Delta R \sim 6$ Å would not consistent with the presence of vacant sites, thus the second hypothesis may be the most plausible.

4.2. Yttrium association with hectorite in coprecipitation and adsorption experiments and consequences for trivalent actinides in HLW repositories

Hectorite formed by condensation of Si tetrahedral sheets on either sides of the brucite precursor and the presence of Y(III) did not have any significant influence on the synthesis protocol (Finck et al., 2009). Furthermore, P EXAFS data indicate that the Y(III) local environment evolved from octahedral brucite like in YcopBru to octahedral clay like in YcopHt. Based on *d*(Mg O) and *d*(Mg Mg) in brucite (Catti et al., 1995) and in hectorite (Seidl and Breu, 2005), the size of the octahedral site decreased during the hectorite crystallization. This may best explain that the first ligand shell in YcopBru consisting of one O shell was split into two subshells in YcopHt, which is indicative of a strong deformation of the YO_6 octahedron. Y(III) is also shifted in the out of plane direction, similarly to YcopBru. Upon contact with pre formed hectorite, Y(III) forms inner sphere surface complexes at the adsorbent surface, thereby loosing part of its hydration sphere. Polarized XAS data indicate that Y(III) binds the octahedral sheet of hectorite sharing edges with Mg octahedra and corner with Si tetrahedra. The formation of such complexes represents another relevant immobilization mechanism. Compared to incorporation within the bulk structure, the re mobilization of surface adsorbed Y(III) can possibly be easier in case of change in geochemical conditions. The formation of such surface complexes in the coprecipitation experiment is marginal.

Trivalent yttrium is of same charge and of size very close to that of trivalent actinides (An(III)). In deep disposal sites, hectorite is expected to form in aqueous environments upon HLW glass alteration, and thus in the presence of dissolved An(III) species. This investigation provides evidences that Y(III), and thus An(III), can substitute for Mg(II) at octahedral sites for smectite prepared in the laboratory, and it can be anticipated that similar incorporation mechanism within smectite in the HLW glass alteration layer may operate as well. Besides coprecipitation, other relevant mechanisms may result in structural incorporation of An(III) within smectites, such as for example surface retention followed by epitaxial growth. This has been shown to operate for divalent cations (Schlegel et al., 2001; Dähn et al., 2002) and can possibly operate for An(III). Such reaction pathway can be of considerable importance in deep repositories due to the likely simultaneous presence of dissolved Mg (supplied by groundwater) and Si (supplied from altering HLW glass). However, further studies would be needed to verify whether this possible uptake mechanism operates.

Because of their large size, the structural compatibility for An(III) may also be limited and they may be located in low crystallinity domains. Yet, clay destabilization depends on various factors such as pH or composition of the (ground) water. Under the geochemical conditions expected to occur in deep disposal sites (e.g., presence of dissolved silica from altering glass and dissolved cations in groundwater), clay destabilization may be hindered, and thus the An(III) re mobilization

highly limited. Further experimental work would be needed to assess the stability of the immobilized species.

4.3. Yttrium association with nanoparticles mobilized from coprecipitated hectorite

The analysis of sample ColYcopHt indicates first that nanoparticles of various sizes (>450, 125 140 and 50 75 nm) can be mobilized from the bulk dispersion, and the presence of various size fractions agrees with earlier studies on NP separated from hectorite synthesized in the pres ence of lanthanides (Bouby et al., 2012, 2015; Finck et al., 2012). AsFlFFF/ICP MS data indicate a homogeneous Y(III) association with hectorite NP of all sizes in the supernatant, a finding that can only be ex plained by random substitution for Mg within hectorite. Similarly, no Y Y pair could be detected by P EXAFS spectroscopy, suggesting random substitution for octahedral cation within hectorite particles of all sizes (i.e. YcopHt). Consequently, XAS and AsFlFFF/ICP MS data provide in formation that random substitution operates for particles of various sizes. Yet, the size of the cation certainly plays an important role but it is reasonable to assume that some trivalent actinide can substitute for octahedral cations within NP of smectites forming in the HLW glass al teration layer.

5. Concluding remarks

Hectorite was synthesized in the presence of Y(III) used as surrogate for trivalent actinides following a multi step synthesis protocol. No in fluence of this dopant on the nature of the formed solid phases could be detected. Polarized XAS data indicated that Y(III) is located succes sively in an octahedral brucite like and in an octahedral clay like envi ronment. Furthermore, AsFlFFF/ICP MS data showed homogeneous Y(III) association to nanoparticulate hectorite. Thus, this study provides significant evidence that cations of large size, such as the long lived and radiotoxic actinides, can occupy octahedral sites in brucite and in clay minerals, resulting in an efficient immobilization.

It can be anticipated that the size mismatch with cations typically occurring at clay octahedral sites limits the extent of substitution and has an impact on the stability of the incorporated species be cause of site distortion. In this study, experiments were performed considering low concentrations of dopant in order to approach con ditions representative of deep HLW disposal sites and data indicated a random substitution for octahedral cations. This result suggests that the structural strain induced by the substitution may be localized and thus have only a limited impact on the bulk clay crystallinity and thus on the stability.

In this study, experiments were prepared under well defined condi tions in the laboratory and it can be anticipated that the incorporation will operate as well in deep HLW disposal sites. However, groundwater contacting the HLW glass may contain various dissolved species, such as for example dissolved organic carbon, able to bind efficiently RN, and this may have an impact on the availability for the incorporation within neoformed alteration phases. Similarly, the composition of the ground water may have an influence on the (ir)reversibility of the immobiliza tion. During the long term evolution of the repository system, inflow of, e.g., low ionic strength groundwater can in principle mobilize RN bear ing NP such as hectorite nanoparticles and serve as carrier if and only if they are stable under the specific (geo)chemical conditions and if the retention is not reversible. In order to allow for their role in performance assessment of a repository, stability and mobility of NP depending on given geochemical conditions and repository setup need to be scruti nized in dedicated studies.

Acknowledgements

ANKA is acknowledged for provision of synchrotron radiation beam time.

Appendix A. Supplementary data

Supplementary data to this article can be found online at http://dx.doi.org/10.1016/j.clay.2016.11.029.

References

Abdelouas, A., Crovisier, J.-L., Lutze, W., Grambow, B., Dran, J.-C., Müller, R., 1997. Surface layers on a borosilicate nuclear waste glass corroded in $MgCl_2$ solution. J. Nucl. Mater. 240, 100–111.

Ankudinov, A.L., Ravel, B., Rehr, J.J., Conradson, S.D., 1998. Real-space multiple-scattering calculation and interpretation of X-ray-absorption near-edge structure. Phys. Rev. B 58, 7565–7576.

Beall, G.W., Milligan, W.O., Wolcott, H.A., 1977. Structural trends in the lanthanide trihydroxides. J. Inorg. Nucl. Chem. 39, 65–70.

Bianconi, A., Dell Ariccia, M., Gargano, A., Natoli, C.R., 1983. Bond length determination using XANES. In: Bianconi, A., Incoccia, L., Stipcich, S. (Eds.), EXAFS and near Edge Structure. Springer, pp. 57–61.

Bosbach, D., Rabung, T., Brandt, F., Fanghanel, T., 2004. Trivalent actinide coprecipitation with powellite ($CaMoO_4$): secondary solid solution formation during HLW borosilicate-glass dissolution. Radiochim. Acta 92, 639–643.

Bouby, M., Geckeis, H., Geyer, F., 2008. Application of asymmetric flow field-flow fractionation (AsFlFFF) coupled to inductively coupled plasma mass spectrometry (ICPMS) to the quantitative characterization of natural colloids and synthetic nanoparticles. Anal. Bioanal. Chem. 392, 1447–1457.

Bouby, M., Geckeis, H., Lutzenkirchen, J., Mihai, S., Schafer, T., 2011. Interaction of bentonite colloids with Cs, Eu, Th and U in presence of humic acid: a flow field-flow fractionation study. Geochim. Cosmochim. Acta 75, 3866–3880.

Bouby, M., Finck, N., Geckeis, H., 2012. Flow field-flow fractionation (FlFFF) coupled to sensitive detection techniques: a way to examine radionuclide interactions with nanoparticles. Mineral. Mag. 76, 2709–2721.

Bouby, M., Finck, N., Geckeis, H., 2015. Synthetic smectite colloids: characterization of nanoparticles after Co-precipitation in the presence of lanthanides and tetravalent elements (Zr, Th). Chromatography 2, 545.

Bradbury, M.H., Baeyens, B., 2002. Sorption of Eu on Na- and Ca-montmorillonites: experimental investigations and modelling with cation exchange and surface complexation. Geochim. Cosmochim. Acta 66, 2325–2334.

Brandt, H., Bosbach, D., Panak, P.J., Fanghänel, T., 2007. Structural incorporaion of Cm(III) in trioctahedral smectite hectorite: a time-resolved laser fluorescence spectroscopy (TRLFS) study. Geochim. Cosmochim. Acta 71, 145–154.

Catti, M., Ferraris, G., Hull, S., Pavese, A., 1995. Static compression and H-disorder in brucite, Mg(OH)(2), to 11 GPA - a powder neutron-diffraction study. Phys. Chem. Miner. 22, 200–206.

Crançon, P., Pili, E., Charlet, L., 2010. Uranium facilitated transport by water-dispersible colloids in field and soil columns. Sci. Total Environ. 408, 2118–2128.

Curti, E., Crovisier, J.L., Morvan, G., Karpoff, A.M., 2006. Long-term corrosion of two nuclear waste reference glasses (MW and SON68): a kinetic and mineral alteration study. Appl. Geochem. 21, 1152–1168.

Dähn, R., Scheidegger, A.M., Manceau, A., Schlegel, M.L., Baeyens, B., Bradbury, M.H., Morales, M., 2002. Neoformation of Ni phyllosilicate upon Ni uptake on montmorillonite: a kinetics study by powder and polarized extended X-ray absorption fine structure spectroscopy. Geochim. Cosmochim. Acta 66, 2335–2347.

Dardenne, K., Schäfer, T., Lindqvist-Reis, P., Denecke, M.A., Plaschke, M., Rothe, J., Kim, J.I., 2002. Low temperature XAFS investigation on the lutetium binding changes during the 2-line Ferrihydrite alteration process. Environ. Sci. Technol. 36, 5092–5099.

Dekov, V.M., Kamenov, G.D., Stummeyer, J., Thiry, M., Savelli, C., Shanks, W.C., Fortin, D., Kuzmann, E., Vertes, A., 2007. Hydrothermal nontronite formation at eolo seamount (Aeolian volcanic arc, Tyrrhenian Sea). Chem. Geol. 245, 103–119.

Díaz-Moreno, S., Muñoz-Páez, A., Chaboy, J., 2000. X-ray absorption spectroscopy (XAS) study of the hydration structure of yttrium(III) cations in liquid and glassy states: eight or nine-fold coordination? J. Phys. Chem. A 104, 1278–1286.

Dubascoux, S., Le Hecho, I., Gautier, M.P., Lespes, G., 2008. On-line and off-line quantification of trace elements associated to colloids by As-Fl-FFF and ICP-MS. Talanta 77, 60–65.

Finck, N., Schlegel, M.L., Bosbach, D., 2009. Sites of Lu(III) Sorbed to and coprecipitated with hectorite. Environ. Sci. Technol. 43, 8807–8812.

Finck, N., Bouby, M., Dardenne, K., Geckeis, H., 2012. Characterization of Eu(III) co-precipitated with and adsorbed on hectorite: from macroscopic crystallites to nanoparticles. Mineral. Mag. 76, 2723–2740.

Finck, N., Dardenne, K., Geckeis, H., 2015a. Am(III) coprecipitation with and adsorption on the smectite hectorite. Chem. Geol. 409, 12–19.

Finck, N., Schlegel, M.L., Bauer, A., 2015b. Structural iron in dioctahedral and trioctahedral smectites: a polarized XAS study. Phys. Chem. Miner. 42, 847–859.

Geckeis, H., Lützenkirchen, J., Polly, R., Rabung, T., Schmidt, M., 2013. Mineral–water interface reactions of actinides. Chem. Rev. 113, 1016–1062.

Güven, N., 1988. Smectites. In: Bailley, S.W. (Ed.), Hydrous Phyllosilicates (exclusive of micas). Mineralogical Society of America, Washington DC, pp. 497–559.

Hassellöv, M., Lyvén, B., Haraldsson, C., Sirinawin, W., 1999. Determination of continuous size and trace element distribution of colloidal material in natural water by on-line coupling of flow field-flow fractionation with ICPMS. Anal. Chem. 71, 3497–3502.

Jollivet, P., Frugier, P., Parisot, G., Mestre, J.P., Brackx, E., Gin, S., Schumacher, S., 2012. Effect of clayey groundwater on the dissolution rate of the simulated nuclear waste glass SON68. J. Nucl. Mater. 420, 508–518.

Kim, J.I., Grambow, B., 1999. Geochemical assessement of actinide isolation in a German salt repository environment. Eng. Geol. 52, 221–230.
Malvestuto, A., Carboni, R., Boscherini, F., D'Acapito, F., Spiga, S., Fanciulli, M., Dimoulas, A., Vellianitis, G., Mavrou, G., 2005. X-ray absorption study of the growth of Y_2O_3 on Si(001). Phys. Rev. B 71, 075318.
Manceau, A., Bonnin, D., Stone, W.E.E., Sanz, J., 1990. Distribution of Fe in the octahedral sheet of trioctahedral micas by polarized EXAFS. Phys. Chem. Miner. 17, 363–370.
Manceau, A., Chateigner, D., Gates, W.P., 1998. Polarized EXAFS, distance-valence least-squares modeling (DVLS), and quantitative texture analysis approaches to the structural refinement of Garfield nontronite. Phys. Chem. Miner. 25, 347–365.
Meunier, A., 2005. Clays. Springer.
Mitric, M., Kremenovic, A., Dimitrijevic, R., Rodic, D., 1997. Structure and microstructure of $Sm_xY_{2-x}O_3$. Solid State Ionics 101–103 (Part 1), 495–501.
Novikov, A.P., Kalmykov, S.N., Utsunomiya, S., Ewing, R.C., Horreard, F., Merkulov, A., Clark, S.B., Tkachev, V.V., Myasoedov, B.F., 2006. Colloid transport of plutonium in the far-field of the Mayak production association, Russia. Science 314, 638–641.
Pieper, H., 2005. Kristallchemischer Einbau trivalenter f-Elemente in trioktaedrische Smectite. Wissenschaftlische Berichte FZKA 7188. Forschungszentrum Karlsruhe GmbH, Karlsruhe (Germany).
Ravel, B., 2000. EXAFS analysis with feff and feffit. Commentary. Part 2 (New York).
Ravel, B., Newville, M., 2005. ATHENA, ARTEMIS, HEPHAESTUS: data analysis for X-ray absorption spectroscopy using IFEFFIT. J. Synchrotron Radiat. 12, 537–541.
Rothe, J., Butorin, S., Dardenne, K., Denecke, M.A., Kienzler, B., Loble, M., Metz, V., Seibert, A., Steppert, M., Vitova, T., Walther, C., Geckeis, H., 2012. The INE-Beamline for actinide science at ANKA. Rev. Sci. Instrum. 83, 043105.
Schimpf, E.M., Caldwell, K., Giddings, J.C., 2000. Field-Flow Fractionation Handbook. Wiley.
Schlegel, M.L., 2008. Polarized EXAFS characterization of the sorption mechanism of yttrium on hectorite. Radiochim. Acta 96, 667–672.
Schlegel, M.L., Descostes, M., 2009. Uranium uptake by hectorite and montmorillonite: a solution chemistry and polarized EXAFS study. Environ. Sci. Technol. 43, 8593–8598.
Schlegel, M.L., Manceau, A., 2013. Binding mechanism of Cu(II) at the clay-water interface by powder and polarized EXAFS spectroscopy. Geochim. Cosmochim. Acta 113, 113–124.
Schlegel, M.L., Manceau, A., Chateigner, D., Charlet, L., 1999. Sorption of metal ions on clay minerals I. Polarized EXAFS evidence for the adsorption of Co on the edges of hectorite particles. J. Colloid Interface Sci. 215, 140–158.
Schlegel, M.L., Manceau, A., Charlet, L., Hazemann, J.L., 2001. Adsorption mechanisms of Zn on hectorite as a function of time, pH, and ionic strength. Am. J. Sci. 301, 798–830.
Schlegel, M.L., Pointeau, I., Coreau, N., Reiller, P., 2004. Mechanism of europium retention by calcium silicate hydrates: an EXAFS study. Environ. Sci. Technol. 38, 4423–4431.
Seidl, W., Breu, J., 2005. Single crystal structure refinement of tetramethylammonium-hectorite. Z. Kristallogr. 220, 169–176.
Severmann, S., Mills, R.A., Palmer, M.R., Fallick, A.E., 2004. The origin of clay minerals in active and relict hydrothermal deposits. Geochim. Cosmochim. Acta 68, 73–88.
Shannon, R.D., 1976. Revised effective ionic radii and systematic studies of interatomic distances in halides and chalcogenides. Acta Crystallogr. A 32, 751–767.
Stumpf, T., Marques Fernandes, M., Walther, C., Dardenne, K., Fanghänel, T., 2006. Structural characterization of Am incorporated into calcite: a TRLFS and EXAFS study. J. Colloid Interface Sci. 302, 240–245.
Stumpf, T., Curtius, H., Walther, C., Dardenne, K., Ufer, K., Fanghänel, T., 2007. Incorporation of Eu(III) into Hydrotalcite: a TRLFS and EXAFS study. Environ. Sci. Technol. 41, 3186–3191.
Teo, B.K., 1986. EXAFS: Basic Principles and Data Analysis. Springer, Berlin Heidelberg.
Thien, B., Godon, N., Hubert, F., Angéli, F., Gin, S., Ayral, A., 2010. Structural identification of a trioctahedral smectite formed by the aqueous alteration of a nuclear glass. Appl. Clay Sci. 49, 135–141.
Utsunomiya, S., Kersting, A.B., Ewing, R.C., 2009. Groundwater nanoparticles in the far-field at the Nevada test site: mechanism for radionuclide transport. Environ. Sci. Technol. 43, 1293–1298.
Zimmer, P., Bohnert, E., Bosbach, D., Kim, J.I., Althaus, E., 2002. Formation of secondary phases after long-term corrosion of simulated HLW glass in brine solutions at 190 °C. Radiochim. Acta 90, 529–535.
Zwicky, H.U., Grambow, B., Magrabi, C., Aerne, E.T., Bradley, R., Barnes, B., Graber, T., Mohos, M., Werme, L.C., 1989. Corrosion behaviour of British Magnox waste glass in pure water. MRS Proc. 127, 129–136.